optica

Monolithic quantum-dot distributed feedback laser array on silicon

YI WANG,[1,†] SIMING CHEN,[2,†,*] YING YU,[1] LIDAN ZHOU,[1] LIN LIU,[1] CHUNCHUAN YANG,[1] MENGYA LIAO,[2] MINGCHU TANG,[2] ZIZHUO LIU,[2] JIANG WU,[2] WEI LI,[4] IAN ROSS,[4] ALWYN J. SEEDS,[2] HUIYUN LIU,[2,5] AND SIYUAN YU[1,3,6]

[1]*State Key Laboratory of Optoelectronic Materials and Technologies, Sun Yat-sen University, Guangzhou 510275, China*
[2]*Department of Electronic and Electrical Engineering, University College London, London WC1E 7JE, UK*
[3]*Department of Electronic and Electrical Engineering, University of Bristol, Bristol BS8 1UB, UK*
[4]*Department of Electronic and Electrical Engineering, University of Sheffield, Sheffield S1 3JD, UK*
[5]*e-mail: huiyun.liu@ucl.ac.uk*
[6]*e-mail: S.Yu@bristol.ac.uk*
Corresponding author: siming.chen@ucl.ac.uk

Electrically pumped lasers directly grown on silicon are key devices interfacing silicon microelectronics and photonics. We report here, for the first time, to the best of our knowledge, an electrically pumped, room-temperature, continuous-wave (CW) and single-mode distributed feedback laser array fabricated in InAs/GaAs quantum-dot gain material epitaxially grown on silicon. CW threshold currents as low as 12 mA and single-mode side mode suppression ratios as high as 50 dB have been achieved from individual devices in the array. The laser array, compatible with state-of-the-art coarse wavelength division multiplexing (CWDM) systems, has a well-aligned channel spacing of 20 ± 0.2 nm and exhibits a record wavelength covering range of 100 nm, the full span of the O-band. These results indicate that, for the first time, to the best of our knowledge, the performance of lasers epitaxially grown on silicon is elevated to a point approaching real-world CWDM applications, demonstrating the great potential of this technology.

1. INTRODUCTION

The ever-growing data volume being transported in today's on-chip and off-chip networks imposes significant challenges on copper-based interconnects. One promising approach to address this challenge is optical interconnect based on silicon photonics [1,2], which is quickly maturing as a viable technology for metro and short-reach data transmission, due to the potential of low-cost, high-yield, and streamlined manufacturing enabled by the mature complementary metal–oxide–semiconductor (CMOS) fabrication technology. While the majority of photonic functions can now be realized on silicon [3], one key missing component is an efficient silicon-based laser. As an indirect-bandgap semiconductor, silicon is very inefficient in light emission [4,5]. As a result, significant efforts have been devoted to producing silicon-based lasers by integrating direct-bandgap III-V compound semiconductors with silicon using either hybrid or monolithic methods. Although the former approach has been proved to be successful in producing III-V lasers and active components on silicon with device performance comparable to those grown on native III-V substrates [6–11], the monolithic approach

based on epitaxial growth, in the longer term, is more desirable when it comes to mass production, due to its potential in realizing low-cost, high-yield, and reliable manufacturing processes.

However, monolithic growth of III-Vs on Si faces considerable hurdles including large lattice mismatch (4% for GaAs and 8% for InP), difference in thermal expansion coefficients, and polar versus non-polar surfaces, which result in several types of defects such as threading dislocations (TDs), micro-thermal cracks, and antiphase boundaries (APBs), respectively, severely degrading the promise of III-V materials [12]. III-V quantum-dot (QD) structures have become one of the most promising material systems for III-V semiconductor lasers to achieve ultimately superior device performance [13–15]. Coincidentally, QDs have also been proved to be less sensitive to defects than conventional quantum well (QW) structures due to effective carrier localization [16]. It is, therefore, no surprise that researchers in the field of silicon photonics have strived for years to develop monolithically integrated III-V QD light sources on silicon substrates that can exploit the benefits of QD while also being able to fully enjoy the economics of scale promised by monolithic growth. As a result, III-V QD

Fabry–Perot (FP) lasers monolithically grown on Si have made significant progress and have outperformed their QW and bulk counterparts in terms of lower threshold current, higher temperature insensitivity, higher efficiency, and longer lifetime [16–25].

While single channel optical interconnects can operate with silicon-based electrically pumped FP lasers, high-performance applications would require arrays of single-mode lasers with carefully designed cavities that enable wavelength division multiplexing (WDM) [26]. Recently, leveraging a novel selective-area growth technique in confined V-shaped grooves, the growth of high-quality InP-based material directly on buffer-free silicon has been achieved [27]. While the first room-temperature monolithic Si-based InP distributed feedback (DFB) laser array emitting within different wavelength ranges has been reported using this method [28,29], the array can only operate by optical pumping, and its wavelength coverage is limited to 40 nm [29]. In this work, we take another step forward and demonstrate, to the best of knowledge, the first electrically pumped DFB laser array using InAs/GaAs QD gain material epitaxially grown on silicon. The array operates under continuous-wave (CW) conditions at room temperature, and features threshold currents as low as 12 mA, side mode suppression ratios (SMSRs) as high as 50 dB, and a record wavelength covering range of 100 nm, the full span of the O-band, manifesting the great potential of the monolithic approach in real systems applications.

2. DESIGN AND FABRICATION

In this work, an InAs/GaAs QD laser structure [Fig. 1(a)] was directly grown on an n-doped silicon (001) substrate with a 4° off-cut angle towards the [011] plane. To achieve high-quality lasers epitaxially grown on silicon, it is crucial to minimize the impact of TDs generated due to the large lattice mismatch between III-Vs and silicon [5,30–33]. Here, special growth techniques have been developed, in which an AlAs nucleation layer, InGaAs/GaAs dislocation filter layers (DFLs) [19], and

in situ thermal annealing [34] have been utilized following previous optimized conditions [21] to deliver high-quality III-V buffer layers grown directly on Si with low TD density of around 1.2×10^6 cm^{-2} determined by transmission electron microscopy (TEM). Following the III-V buffer layers, a standard p-i-n laser structure was grown. The active region was composed of a seven-layer InAs/InGaAs dots-in-a-well (DWELL) structure separated by 50 nm GaAs spacer layers. Each DWELL layer consists of three monolayers of InAs sandwiched between 2 nm lower and 6 nm upper In$_{0.15}$Ga$_{0.85}$As layers [21]. By virtue of the low TD density in the III-V buffer layers, a near defect-free active region [Fig. 1(b)] was achieved. A room-temperature photoluminescence (PL) emission peaking at 1297 nm was observed with a narrow linewidth of 30 meV, as seen in Fig. 1(c). Good QD uniformity and a QD density of $\sim 3 \times 10^{10}$ cm^{-2} were achieved, as indicated by the atomic force micrograph from an uncapped QD test sample grown on silicon under the same growth conditions. The 3-inch wafer was then diced into smaller pieces and fabricated into broad-area FP lasers (see Section 1 of Supplement 1) and the DFB laser array described in this paper.

Conventionally, the development of a III-V DFB laser involves two epitaxial growth sequences, one for the lower cladding and the active region, the other for the upper cladding and the contact layer following the fabrication of shallow-etched gratings near the waveguide core [35]. Alternatively, a simplified method avoiding complicated regrowth has been developed, in which lateral surface gratings are fabricated simultaneously in the waveguide etching process [36,37]. The gratings are etched to just above the active region to achieve strong photon-grating interactions as well as low optical loss. For InP-based structures, an aluminum-containing stop-etch layer and a chemically selective dry etching recipe are often used together to ensure the etch depth to be precisely above the active region, so as to obtain an accurate modal refractive index and grating coupling coefficient κ. However, in the InAs/GaAs QD material system described above, such a stop-etch process has not been found to date. Therefore, in our design, waveguides with lateral gratings engraved on their sidewalls that penetrated the active region were used. To retain the high repeatability, they were intentionally over-etched to about 500 nm into the lower cladding, as seen in Fig. 2(a). In doing so, an inductively coupled plasma (ICP) etching recipe of ultra-high aspect ratio (>30:1) using the SiCl$_4$/N$_2$ chemistry was developed. Figure 2(c) shows the high-resolution scanning electron microscope (SEM) image of 3.4 µm deep-etched gratings with masks generated by e-beam lithography (EBL). Exploiting such a deep-etching method could enhance the immunity to the variations of the etch depth expected in different batches, which would otherwise result in drift of the modal refractive index leading to detrimental wavelength shifting (see Section 2 of Supplement 1). In addition, as QDs were used in the active region, the negative impact of non-radiative recombination occurring on the ridge surface has been minimized, owing to their improved insensitivity to defects. A simple yet robust fabrication process was therefore achieved.

Typically, sufficiently narrow waveguides are used in DFB lasers to support only the fundamental transverse mode in order to guarantee single-transverse-mode operation. However, given the deep-etched waveguide design, the single-mode waveguide is too narrow to provide sufficient gain, or to ensure a reasonable grating size for good reproducibility. In our design, a waveguide
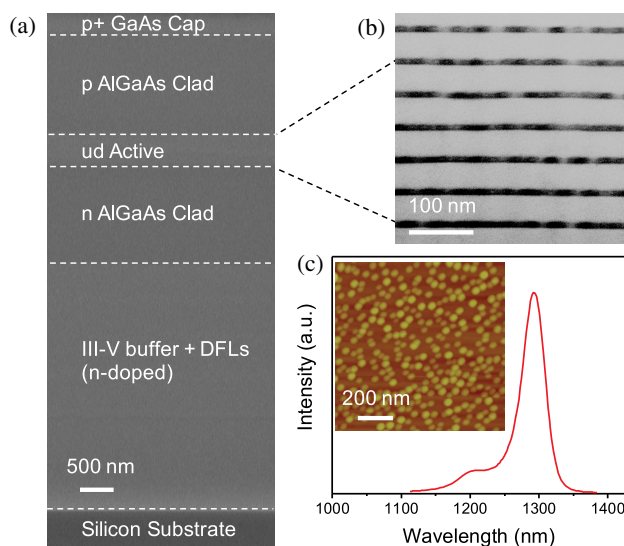

Fig. 1. Material properties of Si-based QD lasers. (a) SEM image of the transverse layer structure of the epi-wafer used in laser fabrication. (b) Bright field STEM image of the active layers. (c) Photoluminescence spectrum of the QD active layers on silicon peaking at 1297 nm. The inset shows the atomic force microscope image of an uncapped QD layer.
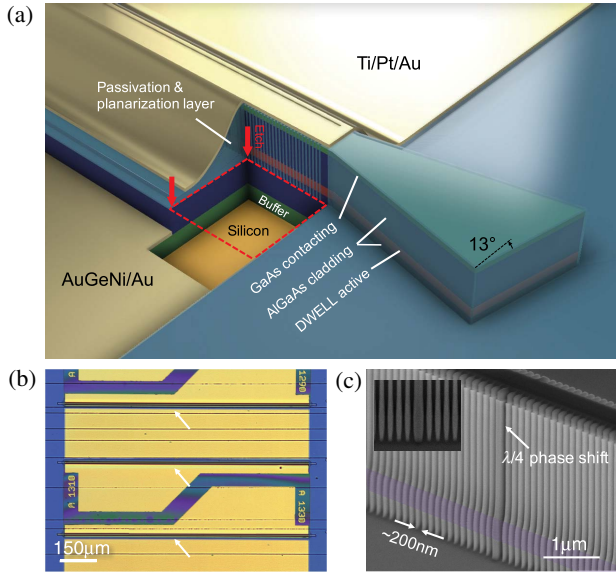
(a)

(b)

(c)

(a)

(b)

Fig. 2. DFB laser array on silicon. (a) Cutaway schematic showing the vertical layer structure, the output coupler, and the etched gratings (not to scale). (b) Regional microscope image of the DFB laser array on silicon. The arrows indicate positions of the ridge waveguides. (c) High-resolution SEM image of the gratings with a $\lambda/4$ phase shift in the middle from a test run. The e-beam resist is still present. Shaded in light purple is the active region. Inset: SEM image of the gratings from a near 90° viewpoint showing the high-quality gratings with almost no residue. The scale bar applies to both images.

Fig. 3. Modal analysis of the DFB laser. (a) Modal refractive indices of the first three modes in deep-etched waveguides of different widths. (b) Optical spectrum of a multimode DFB laser with a waveguide width of 2.2 μm and total length of 1.5 mm, operating above threshold with continuous electrical pumping at room temperature.

width of 2.2 μm supporting the first three transverse modes, as seen in Fig. 3(a), was found to be a good trade-off by showing single-mode lasing in the second-order mode. Having a larger κ compared to the fundamental mode, and being still well confined in the waveguide thanks to the sufficiently wide ridge, the second-order transverse mode can reach threshold first and suppress the fundamental mode from lasing thereafter. Theoretically, κ can be estimated by the difference of refractive indices between two transverse slices of the waveguide [38,39], one slice on the peak and the other on the trough. Furthermore, in contrast to the second-order mode, the third-order mode is more sensitive to surface scattering due to poor confinement, which eventually prevents it from lasing. No signs of lasing in the third-order mode were found experimentally.

The experimental evidence of lasing in the second-order mode was found using DFB lasers with a dimension of 2.2 μm × 1.5 mm. By electrically pumping these lasers to above threshold, two-mode lasing with an extra mode sitting at a wavelength 17 nm longer than the desired mode was observed [Fig. 3(b)], which was in good agreement with the theoretical spacing of 15.5 nm between the TE_{10} and TE_{00} modes. By comparison, the theoretical wavelength spacing between TE_{20} and TE_{10} modes was 26.3 nm. We therefore deduced that the two lasing peaks corresponded to the TE_{10} and TE_{00} modes, respectively. To eliminate the unstable TE_{00} mode, the total length of the grating was decreased to 1.2 mm and 1 mm, thus lowering the total coupling strength and increasing the threshold for the fundamental mode. This design provides robust single-mode operations, which will be shown later in the paper. It should be noted that the second-order mode can be easily converted into the fundamental mode by waveguide mode converters [40],
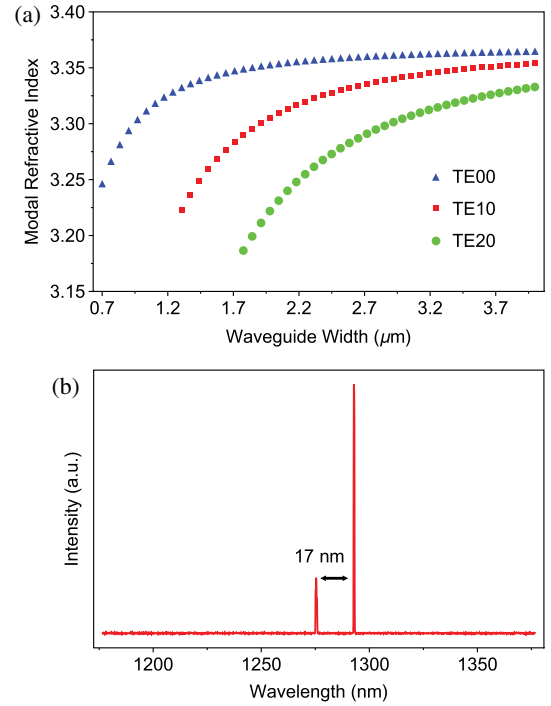
for the purpose of coupling into single-mode waveguides in future versions of the device.

To achieve a suitable κ, low radiation loss, and a reliable fabrication process, the sidewall gratings have been designed as 50:50 first-order, with an intrusion length of 100 nm. A $\lambda/4$ phase shift was placed in the middle of the gratings to force single-longitudinal-mode lasing in the defect mode. The WDM-compatible laser array was achieved by carefully adjusting the grating periods of the lasers in the array. The first-order grating period values p were determined first coarsely, using n_{eff} obtained by numerical simulations and the relation

$$p = \frac{\lambda}{2n_{eff}}. \qquad (1)$$

As seen in the equation, any variations of n_{eff} will lead to corresponding changes in the lasing wavelength λ assuming fixed grating periods, which is inevitable with the presence of simulation and fabrication errors. However, given the linear relation between λ and p, more accurate grating period values can be determined from a calibration batch on the same wafer, including fabrication of coarsely designed DFB lasers and measurement of their lasing wavelengths.

Another important factor for DFB lasers is the suppression of facet backreflections, and failure to do so may cause mode jumping at high currents. Here, owing to the high-aspect-ratio etching process, this problem was tackled simply and cost-effectively by dry-etched antireflection (AR) output couplers instead of additional AR coatings. Generally, by tilting the output facet and widening the waveguide, the facet reflectivity can be greatly reduced due to mode mismatch in the reflected light [41]. However, large
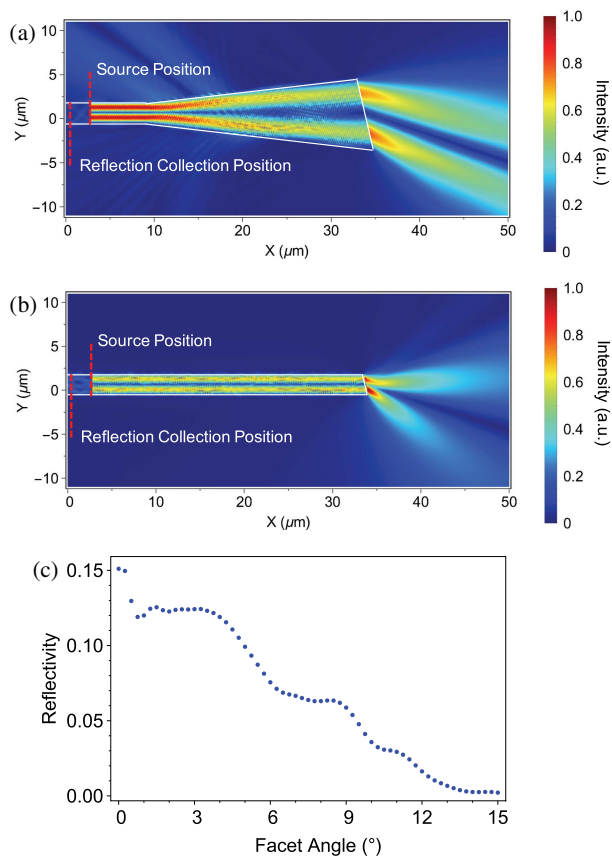
Fig. 4. FDTD simulation result of the output coupler with a TE_{10} modal input showing low reflection back into the waveguide. The waveguide outline, the source position, and the reflection collection position are drawn in the figure, respectively. (a) Beveled output facet with a forward taper. The reflectivity is ∼1%. (b) Beveled output facet without a forward taper. The reflectivity is ∼10%. (c) FDTD simulated reflectivity of the AR output coupler with an 8 μm wide, 25 μm long forward taper attached to the 2.2 μm deep-etched waveguide.

tilting angles and waveguide widths may cause difficulties in coupling. As a trade-off, the combined use of an 8 μm wide, 25 μm long forward taper and a 13° tilted facet successfully decreased the reflection coefficient down to ∼1% and increased the output efficiency up to ∼82%, meanwhile maintaining a reasonable beam profile that can be collected by an optical fiber. The simulation results were obtained by finite-difference time-domain (FDTD) simulations, as shown in Fig. 4. The absorption of the un-pumped output coupler was estimated to be 7% by FDTD simulations, and this was considered acceptable. Successful fabrication of the facet was supported by the high SMSR and high mode stability demonstrated later in the paper. Note that the use of etched facets can also avoid the issue of unpredictable cleaving of off-cut silicon substrates and, more significantly, pave the way towards monolithic laser-waveguide integration by enabling high-performance devices without cleaving. A detailed description of the fabrication process can be found in Supplement 1.

3. RESULTS

To analyze the optical spectrum of the silicon-based WDM DFB laser array, the finished wafer was first diced into independent bars each containing multiple DFB lasers with varying grating periods,

and then placed face-up on a three-axis aligning stage for probe-testing. The individual lasers on the bar were biased with a direct current (DC) source at room temperature (24°C) with no active cooling, and then butt-coupled with a 50 μm/125 μm multimode fiber. CW single-mode lasing was observed. The six-device array produced a wavelength range of 100 nm around the 1300 nm communication band, as seen in Fig. 5(a). A 0.1 nm precision was achieved for the grating period, yielding a channel spacing of 20 ± 0.2 nm, matching well with the standard coarse wavelength division multiplexing (CWDM) grid.

The sub-threshold spectrum of an individual device showing typical $\lambda/4$ phase-shifted DFB laser characteristics is given in Fig. 5(c). The spectrum consists of a 0.8 nm wide bandgap and a central defect mode that would lase at higher currents. The total coupling strength κL for the 1.2 mm long device was estimated by the bandgap width to be around 5. This relatively strong coupling strength could alleviate any residual facet backreflections introduced by fabrication errors, thus improving the single-mode quality. The mode stability is also evident in the light-current-voltage (LIV) curve in Fig. 5(d), where above the 550 A cm⁻² (12 mA) threshold the output power follows a kink-free near-linear curve for the 1 mm long silicon-based DFB laser. The slope efficiency and wall-plug efficiency at 49 mA were calculated to be 0.024 W A⁻¹ and 0.5%, respectively. As the p- and n-electrodes were both fabricated on the epi-side, the current flow could avoid the defect-rich III-V/Si interface, and therefore a slope resistance of around 20 Ω after diode turn-on was achieved. Room-temperature output power per facet exceeded 0.5 mW and 1.5 mW under CW and pulsed conditions of 1 μs pulsewidth and 1% duty ratio, respectively. More information regarding the LIV curves of the array can be found in Section 3 of Supplement 1.

The mode stability of communication-oriented silicon-based DFB lasers has also been characterized in terms of SMSR and temperature-dependent or current-dependent wavelength shift. As plotted in Fig. 6(a), starting from a weak amplified spontaneous emission (ASE) near threshold, the lasing mode quickly reached a high SMSR of ∼50 dB at 2.3 kA cm⁻² (60 mA). The high SMSR value implies a correct combination of the design parameters and the successful fabrication of an etched AR facet. By varying the injection currents, the peak emission wavelength drifted at a rate of 0.03 nm mA⁻¹ or 8.6 pm mW⁻¹ corresponding to a shift of 1.2 nm at 2.3 kA cm⁻² (60 mA), which was well within the CWDM channel window. Temperature-dependent measurement was carried out under a pulsed condition of 1 μs pulsewidth and 1% duty ratio, to minimize the effect of electrical self-heating. As shown in Fig. 6(b), the wavelength thermal drift was fitted to be 0.11 nm °C⁻¹, which meant the CW device temperature at 60 mA was around 35°C (11°C above substrate temperature). The thermal resistance calculated was approximately 50 °C W⁻¹. It is worth mentioning that the data presented above represent the worst-case results, because the lasers were operated epi-side up without substrate thinning (the substrate thickness was 410 μm) and they were not hard-soldered to a high thermal conductivity heatsink. The lasers were also directly probed without wire-bonding. Proper bonding would improve the device performance. The high performance obtained even in such harsh testing conditions further confirmed the potential of this laser array in real application scenarios with demanding environmental requirements.
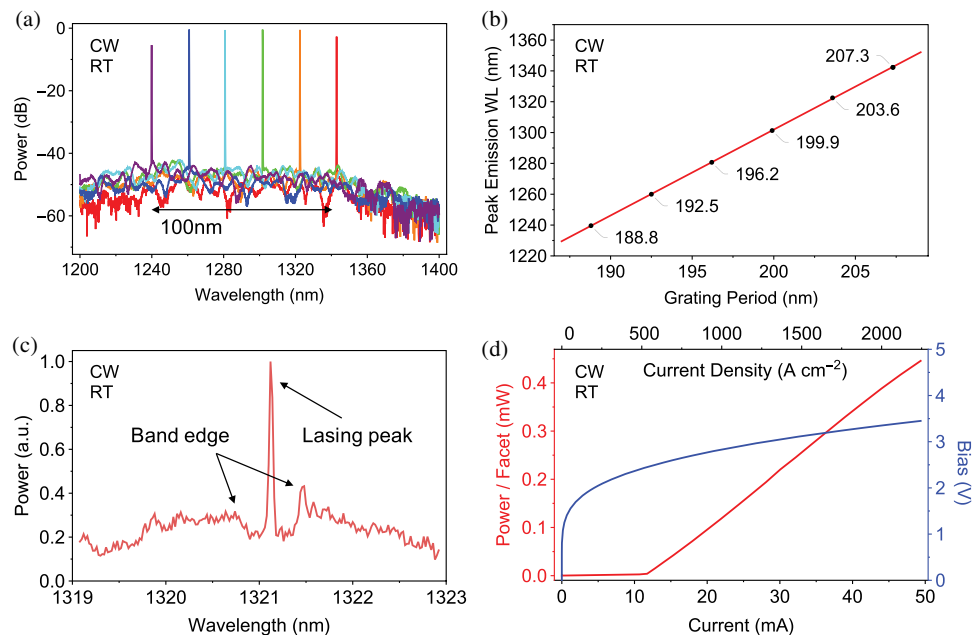
Fig. 5. Continuous-wave test results of the silicon-based DFB laser array at room temperature. (a) Optical spectra of a DFB laser array with different grating periods around their maximum output power levels before saturation at room temperature. Resolution: 0.1 nm. (b) Peak emission wavelengths of the DFB laser array plotted against grating period values. The callouts indicate the corresponding grating period values of the lasers in the array. The wavelengths were obtained at the same current density of 1.9 kA cm^{-2}. (c) Zoomed-in optical spectrum of a single DFB laser operating just below threshold. Resolution: 0.07 nm. (d) Light-current-voltage curve of a single 1 mm long silicon-based DFB laser. The output power was collected at one of the two symmetric facets.
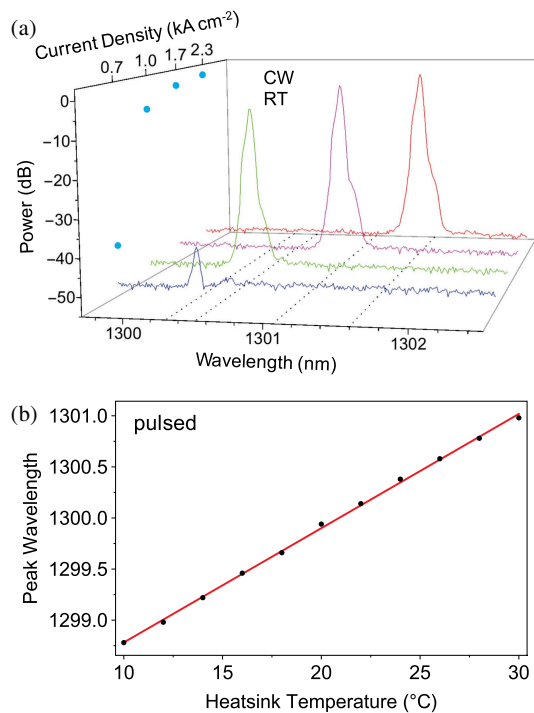
4. CONCLUSION

We have designed and demonstrated, for the first time to the best of our knowledge, an electrically pumped CWDM DFB laser array using InAs/GaAs QD gain materials monolithically grown on a silicon substrate. Operating at room temperature, the DFB laser array exhibited threshold currents as low as 12 mA, SMSRs as high as 50 dB, and a wavelength coverage of 100 nm with a precise channel spacing of 20 ± 0.2 nm. These results meet the CWDM requirements and represent a major step towards fully monolithic silicon-based photonic integrated circuits (PICs) for low-cost and high-performance applications. The Si-based DFB laser technology can also be used for non-communications applications such as on-chip sensing and metrology where integrated single-mode coherent sources are a key part of the functional PICs.

See Supplement 1 for supporting content.

†These authors contributed equally to this work.

Fig. 6. Mode stability test results on one silicon-based DFB laser in the array. (a) Normalized peak power (left panel) and optical spectra of a single DFB laser with different DC currents at room temperature. (b) Linear fit of peak emission wavelengths for the DFB laser driven by a pulsed source of 1 μs pulsewidth and 1% duty cycle at different heatsink temperatures.

REFERENCES

1. D. Miller, "Device requirements for optical interconnects to silicon chips," Proc. IEEE **97**, 1166–1185 (2009).

2. C. Sun, M. Wade, Y. Lee, J. Orcutt, L. Alloatti, M. Georgas, A. Waterman, J. Shainline, R. Avizienis, S. Lin, B. Moss, R. Kumar, F. Pavanello, A. Atabaki, H. Cook, A. Ou, J. Leu, Y. Chen, K. Asanović, R. Ram, M. Popović, and V. Stojanović, "Single-chip microprocessor that communicates directly using light," Nature **528**, 534–538 (2015).

3. M. Deen and P. Basu, *Silicon Photonics* (Wiley, 2012).

4. H. Rong, S. Xu, Y. Kuo, V. Sih, O. Cohen, O. Raday, and M. Paniccia, "Low-threshold continuous-wave Raman silicon laser," Nat. Photonics **1**, 232–237 (2007).

5. D. Liang and J. Bowers, "Recent progress in lasers on silicon," Nat. Photonics **4**, 511–517 (2010).

6. G. Roelkens, L. Liu, D. Liang, R. Jones, A. Fang, B. Koch, and J. Bowers, "III-V/silicon photonics for on-chip and intra-chip optical interconnects," Laser Photon. Rev. **4**, 751–779 (2010).

7. K. Tanabe, K. Watanabe, and Y. Arakawa, "III-V/Si hybrid photonic devices by direct fusion bonding," Sci. Rep. **2**, 349 (2012).

8. S. Keyvaninia, S. Verstuyft, L. Van Landschoot, F. Lelarge, G. Duan, S. Messaoudene, J. Fedeli, T. De Vries, B. Smalbrugge, E. Geluk, J. Bolk, M. Smit, G. Morthier, D. Van Thourhout, and G. Roelkens, "Heterogeneously integrated III-V/silicon distributed feedback lasers," Opt. Lett. **38**, 5434–5437 (2013).

9. G. Crosnier, D. Sanchez, S. Bouchoule, P. Monnier, G. Beaudoin, I. Sagnes, R. Raj, and F. Raineri, "Hybrid indium phosphide-on-silicon nanolaser diode," Nat. Photonics **11**, 297–300 (2017).

10. L. Liu, R. Kumar, K. Huybrechts, T. Spuesens, G. Roelkens, E. Geluk, T. de Vries, P. Regreny, D. Van Thourhout, R. Baets, and G. Morthier, "An ultra-small, low-power, all-optical flip-flop memory on a silicon chip," Nat. Photonics **4**, 182–187 (2010).

11. Z. Wang, K. Van Gasse, V. Moskalenko, S. Latkowski, E. Bente, B. Kuyken, and G. Roelkens, "A III-V-on-Si ultra-dense comb laser," Light Sci. Appl. **6**, e16260 (2016).

12. J. Ayers, T. Kujofsa, P. Rango, and J. Raphael, *Heteroepitaxy of Semiconductors: Theory, Growth, and Characterization*, 2nd ed. (CRC Press, 2017).

13. Y. Arakawa and H. Sakaki, "Multidimensional quantum well laser and temperature dependence of its threshold current," Appl. Phys. Lett. **40**, 939–941 (1982).

14. M. Sugawara and M. Usami, "Quantum dot devices: handling the heat," Nat. Photonics **3**, 30–31 (2009).

15. K. Nishi, K. Takemasa, M. Sugawara, and Y. Arakawa, "Development of quantum dot lasers for data-com and silicon photonics applications," IEEE J. Sel. Top. Quantum Electron. **23**, 1–7 (2017).

16. Z. Mi, J. Yang, P. Bhattacharya, G. Qin, and Z. Ma, "High-performance quantum dot lasers and integrated optoelectronics on Si," Proc. IEEE **97**, 1239–1249 (2009).

17. A. Liu, C. Zhang, J. Norman, A. Snyder, D. Lubyshev, J. Fastenau, A. Liu, A. Gossard, and J. Bowers, "High performance continuous wave 1.3 μm quantum dot lasers on silicon," Appl. Phys. Lett. **104**, 041104 (2014).

18. A. Liu, S. Srinivasan, J. Norman, A. Gossard, and J. Bowers, "Quantum dot lasers for silicon photonics [Invited]," Photon. Res. **3**, B1–B9 (2015).

19. M. Tang, S. Chen, J. Wu, Q. Jiang, K. Kennedy, P. Jurczak, M. Liao, R. Beanland, A. Seeds, and H. Liu, "Optimizations of defect filter layers for 1.3-μm InAs/GaAs quantum-dot lasers monolithically grown on Si substrates," IEEE J. Sel. Top. Quantum Electron. **22**, 50–56 (2016).

20. H. Liu, T. Wang, Q. Jiang, R. Hogg, F. Tutu, F. Pozzi, and A. Seeds, "Long-wavelength InAs/GaAs quantum-dot laser diode monolithically grown on Ge substrate," Nat. Photonics **5**, 416–419 (2011).

21. S. Chen, W. Li, J. Wu, Q. Jiang, M. Tang, S. Shutts, S. Elliott, A. Sobiesierski, A. Seeds, I. Ross, P. Smowton, and H. Liu, "Electrically pumped continuous-wave III-V quantum dot lasers on silicon," Nat. Photonics **10**, 307–311 (2016).

22. A. Liu, J. Peters, X. Huang, D. Jung, J. Norman, M. Lee, A. Gossard, and J. Bowers, "Electrically pumped continuous-wave 1.3 μm quantum-dot lasers epitaxially grown on on-axis (001) GaP/Si," Opt. Lett. **42**, 338–341 (2017).

23. S. Chen, M. Liao, M. Tang, J. Wu, M. Martin, T. Baron, A. Seeds, and H. Liu, "Electrically pumped continuous-wave 1.3 μm InAs/GaAs quantum dot lasers monolithically grown on on-axis Si (001) substrates," Opt. Express **25**, 4632–4639 (2017).

24. M. Liao, S. Chen, S. Huo, S. Chen, J. Wu, M. Tang, K. Kennedy, W. Li, S. Kumar, M. Martin, T. Baron, C. Jin, I. Ross, A. Seeds, and H. Liu, "Monolithically integrated electrically pumped continuous-wave III-V quantum dot light sources on silicon," IEEE J. Sel. Top. Quantum Electron. **23**, 1–10 (2017).

25. Y. Wan, J. Norman, Q. Li, M. Kennedy, D. Liang, C. Zhang, D. Huang, Z. Zhang, A. Liu, A. Torres, D. Jung, A. Gossard, E. Hu, K. Lau, and J. Bowers, "1.3 μm submilliamp threshold quantum dot micro-lasers on Si," Optica **4**, 940–944 (2017).

26. J. Palais, *Fiber Optic Communications* (Prentice-Hall, 2005).

27. C. Merckling, N. Waldron, S. Jiang, W. Guo, N. Collaert, M. Caymax, E. Vancoille, K. Barla, A. Thean, M. Heyns, and W. Vandervorst, "Heteroepitaxy of InP on Si (001) by selective-area metal organic vapor-phase epitaxy in sub-50 nm width trenches: the role of the nucleation layer and the recess engineering," J. Appl. Phys. **115**, 023710 (2014).

28. Z. Wang, B. Tian, M. Pantouvaki, W. Guo, P. Absil, J. Van Campenhout, C. Merckling, and D. Van Thourhout, "Room-temperature InP distributed feedback laser array directly grown on silicon," Nat. Photonics **9**, 837–842 (2015).

29. B. Tian, Z. Wang, M. Pantouvaki, P. Absil, J. Van Campenhout, C. Merckling, and D. Van Thourhout, "Room temperature O-band DFB laser array directly grown on (001) silicon," Nano Lett. **17**, 559–564 (2016).

30. Z. Zhou, B. Yin, and J. Michel, "On-chip light sources for silicon photonics," Light Sci. Appl. **4**, e358 (2015).

31. J. Wu, S. Chen, A. Seeds, and H. Liu, "Quantum dot optoelectronic devices: lasers, photodetectors and solar cells," J. Phys. D **48**, 363001 (2015).

32. Q. Li and K. Lau, "Epitaxial growth of highly mismatched III-V materials on (001) silicon for electronics and optoelectronics," Prog. Cryst. Growth Charact. Mater. **63**, 105–120 (2017).

33. Z. Wang, A. Abbasi, U. Dave, A. De Groote, S. Kumari, B. Kunert, C. Merckling, M. Pantouvaki, Y. Shi, B. Tian, K. Van Gasse, J. Verbist, R. Wang, W. Xie, J. Zhang, Y. Zhu, J. Bauwelinck, X. Yin, Z. Hens, J. Van Campenhout, B. Kuyken, R. Baets, G. Morthier, D. Van Thourhout, and G. Roelkens, "Novel light source integration approaches for silicon photonics," Laser Photon. Rev. **11**, 1700063 (2017).

34. J. Orchard, S. Shutts, A. Sobiesierski, J. Wu, M. Tang, S. Chen, Q. Jiang, S. Elliott, R. Beanland, H. Liu, P. Smowton, and D. Mowbray, "*In situ* annealing enhancement of the optical properties and laser device performance of InAs quantum dots grown on Si substrates," Opt. Express **24**, 6196–6202 (2016).

35. S. Chuang, *Physics of Photonic Devices* (Wiley, 2009).

36. H. Kim, J. Wiedmann, K. Matsui, S. Tamura, and S. Arai, "1.5-μm-wavelength distributed feedback lasers with deeply etched first-order vertical grating," Jpn. J. Appl. Phys. **40**, L1107–L1109 (2001).

37. K. Mathwig, W. Kaiser, A. Somers, J. Reithmaier, A. Forchel, K. Ohira, S. Ullah, and S. Arai, "DFB lasers with deeply etched vertical grating based on InAs-InP quantum-dash structures," IEEE Photonics Technol. Lett. **19**, 264–266 (2007).

38. A. Laakso, J. Karinen, and M. Dumitrescu, "Modeling and design particularities for distributed feedback lasers with laterally-coupled ridge-waveguide surface gratings," Proc. SPIE **7933**, 79332K (2011).

39. Y. Cao, X. Hu, X. Luo, J. Song, Y. Cheng, C. Li, C. Liu, H. Wang, L. Tsung-Yang, G. Lo, and Q. Wang, "Hybrid III-V/silicon laser with laterally coupled Bragg grating," Opt. Express **23**, 8800–8808 (2015).

40. D. Chen, X. Xiao, L. Wang, Y. Yu, W. Liu, and Q. Yang, "Low-loss and fabrication tolerant silicon mode-order converters based on novel compact tapers," Opt. Express **23**, 11152–11159 (2015).

41. B. Jaskorzynska, L. Thylén, and J. Nilsson, "Modal reflectivity of uptapered, tilted-facet, and antireflection-coated diode-laser amplifiers," J. Opt. Soc. Am. B **8**, 484–493 (1991).